RESEARCH ARTICLE SUMMARY

VOLCANOLOGY

The tangled tale of Kīlauea's 2018 eruption as told by geochemical monitoring

Cheryl Gansecki*, R. Lopaka Lee, Thomas Shea, Steven P. Lundblad, Ken Hon, Carolyn Parcheta

INTRODUCTION: Fissures sliced through Kīlauea Volcano's lower east rift zone on 3 May 2018, eventually engulfing hundreds of structures in lava flows and triggering a collapse at the summit. During the eruption, we employed a rapid routine for geochemical analysis of lava, developed over 6 years of monitoring the prior continuous eruption at Kīlauea. The application of this routine elevated lava chemistry to a near real-time data stream in eruption monitoring, similar to seismic and geodetic data. It provided an unparalleled opportunity to understand changes in magma characteristics during a rapidly evolving eruptive crisis.

RATIONALE: Lava chemistry provides vital information on the underground sources of magma, eruptive conditions, temperature, and physical properties of lava flows. However, analytical techniques are typically slow, leaving chemical analysis of lava as a retrospective tool in the volcano sciences. We developed an analytical procedure to characterize the geochemistry of lava within a few hours of sample collection, allowing us to identify a specific suite of major and trace elements that track lava compositions and estimate lava temperatures through chemical geothermometers. This information was used to inform response teams of shifts in eruptive conditions.

RESULTS: The initial fissures erupted low volumes of chemically evolved basaltic lavas from 3 to 9 May, which were viscous and cool (~1110°C). On 13 May we detected less-evolved compositions and an increase in inferred lava temperatures (~1130°C). We informed science and response teams that the arrival of more fluid and voluminous lava was likely. Beginning 17 to 18 May, the lava from the primary fissures became increasingly less chem-

ically evolved, hotter, and more fluid. By 28 May, activity focused on a single vent (fissure 8). This vent fed a massive outpouring of hotter (~1145°C) lava that continued for more than 2 months. During this stage, lavas became slightly hotter and lost the cargo of lower-temperature minerals that were initially abundant. The lava carried olivine crystals with unusually high MgO, indicative of the presence of much hotter magma (>1270°C) somewhere in the plumbing system. A second dominant olivine population formed in cooler magma similar to what was being erupted previously at the summit lava lake.

We also identified simultaneous, but more explosive, repetitive outbursts of andesite lava. This highly viscous and evolved composition, not previously known from Kīlauea, erupted at low temperatures (1060° to 1090°C) on a fissure offset from the other eruption fissures. The chemical and mineralogical fingerprint of this lava was also detected at other fissures several kilometers from the andesite vent.

CONCLUSION: Analysis of the data during the eruption revealed that at least three different sources of magma were feeding the eruption. The first two were the chemically evolved basalt of the initial fissures and the highly viscous andesite. Both are volumetrically minor sources that represent distinct pockets of old residual magma from Kīlauea's east rift zone that evolved for more than 55 years, cooling and crystallizing at depth. The third and volumetrically more substantial source was less-evolved and hotter basalt of fissure 8. This source was similar in composition to the magma erupted at Kīlauea in the years before 2018 and was ultimately derived from the summit region. Draining and collapse of the summit by this voluminous eruption may have stirred up deeper, hotter parts of the summit magma system and sent mixed magma down the rift. By the final 20 days of the eruption, most magma stored within the active rift system had flushed out. Post-eruption analyses done by traditional geochemical methods confirmed that the rapid-response routine produced comparable data and validated the models proposed during the active eruption. Our work has demonstrated that geochemical analyses of lava samples in near-real-time can yield critical information that enhances hazard assessments and risk mitigation during an eruption. ∎
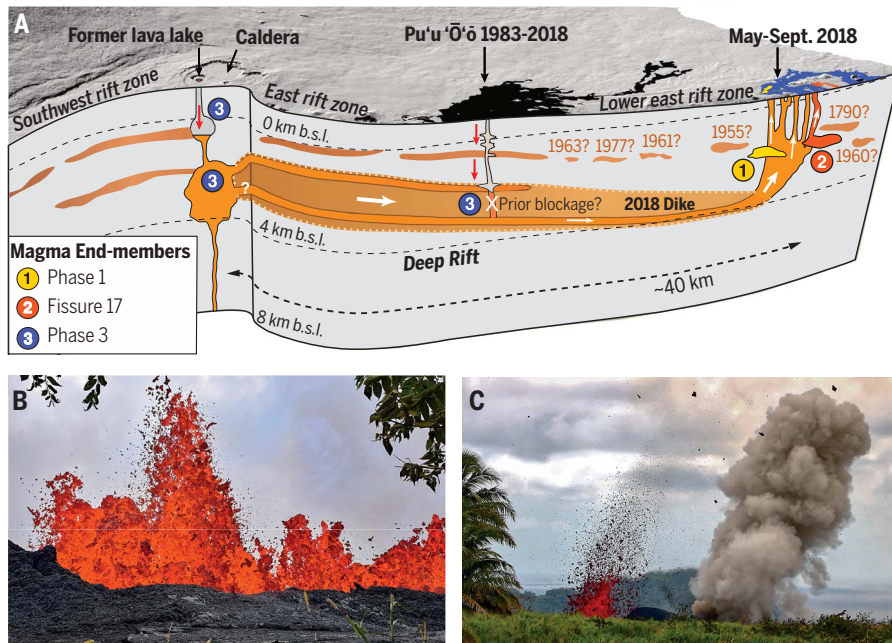
The 2018 lower east rift zone eruption of Kīlauea Volcano with inferred magma sources and pathways. (**A**) Simplified model of Kīlauea's magma system feeding the 2018 lower east rift zone eruption and locations of hypothesized magma end-members (b.s.l., below sea level). (**B**) Fluid basalt erupting from fissure 20 on 20 May 2018. (**C**) Fissure 17 erupting andesite more explosively 800 m away. Photos by U.S. Geological Survey.

RESEARCH ARTICLE

VOLCANOLOGY

The tangled tale of Kīlauea's 2018 eruption as told by geochemical monitoring

Cheryl Gansecki[1]*, R. Lopaka Lee[2], Thomas Shea[3], Steven P. Lundblad[1], Ken Hon[1], Carolyn Parcheta[2]

Changes in magma chemistry that affect eruptive behavior occur during many volcanic eruptions, but typical analytical techniques are too slow to contribute to hazard monitoring. We used rapid energy-dispersive x-ray fluorescence analysis to measure diagnostic elements in lava samples within a few hours of collection during the 2018 Kīlauea eruption. The geochemical data provided important information for field crews and civil authorities in advance of changing hazards during the eruption. The appearance of hotter magma was recognized several days before the onset of voluminous eruptions of fast-moving flows that destroyed hundreds of homes. We identified, in near real-time, interactions between older, colder, stored magma—including the unexpected eruption of andesite—and hotter magma delivered during dike emplacement.

Chemical analysis of lava provides a wealth of information about physical properties of flows, eruptive conditions, magma transport, and magma storage. Typically, analyses trail events by weeks to months, which inhibits combining geochemical data with live streams of seismic, geodetic, gas chemistry data, and field observations. Chemical changes have particular significance at Kīlauea Volcano, where the initial phases of many fissure eruptions are dominated by differentiated lava from past eruptions that is stored in the rift zone [e.g., (1–3)]. The degree of fractionation, the volume of stored magma, and the amount of mixing with intruding magma are highly variable and exert substantial control on eruption behavior. In long-lived rift eruptions such as Pu'u 'Ō'ō (1983–2018), fractionated magma may take several years to flush out, before lava compositions become dominated by the newer magma and stabilize (4). During the 2018 Kīlauea lower East Rift Zone (LERZ) eruption, the collection and rapid chemical analysis of lava samples were key to identifying and monitoring properties of lava and deciphering eruptive processes as they occurred.

The U.S. Geological Survey (USGS) Hawaiian Volcano Observatory (HVO) and the University of Hawaii at Hilo (UH Hilo) have partnered since 2012 to develop a rapid analytical protocol to characterize lava from active eruptions within a few hours of collection. The procedure developed during the continuous eruption of Pu'u 'Ō'ō rapidly analyzes a limited suite of trace elements and major elements

to identify changes in maximum lava temperatures, crystal fractionation trends, storage, and source origins. The chemical data are easily integrated with other monitoring data sources during an eruptive crisis, allowing interpretations and hazard assessments in real time not previously possible.

2018 Kīlauea eruption

The collapse of the long-lived Pu'u 'Ō'ō vent of Kīlauea volcano on the Island of Hawai'i on

30 April was followed by downrift propagation of a dike into the LERZ (5). On 3 May, eruptive fissures opened in the Leilani Estates subdivision west of Pohoiki Road. Fifteen fissure segments erupted along a single fracture trend during the first week, followed by an eruptive pause beginning on 9 May, although local earthquakes and deformation continued (5). On 12 May, new fissures opened east of Pohoiki Road downrift along the same trend, eventually extending 6.8 km in total length along 24 fissures (Fig. 1) (5). Only one fissure, 17, opened offset from the others (Fig. 1). Lava output increased rapidly as the main eruptive activity shifted back uprift through May. Massive flows from fissure 8 commenced on 28 May and remained vigorously active until 4 August (5). The last active lava was observed in the fissure 8 vent on 5 September. Effusion rates up to 200 m³/s (dense-rock equivalent) produced an estimated total of 0.8 to 1.0 km³ of lava, making this the largest LERZ eruption in 200 years (5).

The timing and pattern of 2018 LERZ fissure eruptions define four general eruptive phases. The first three eruptive phases coincide largely with the changes in composition that we describe below, whereas phase 4 produced no lava to analyze. We also consider the eruption of fissure 17, and the later reactivation of certain fissures (particularly 13, 18, 19, and 22), as discrete events that warrant separate consideration given their compositional differences.
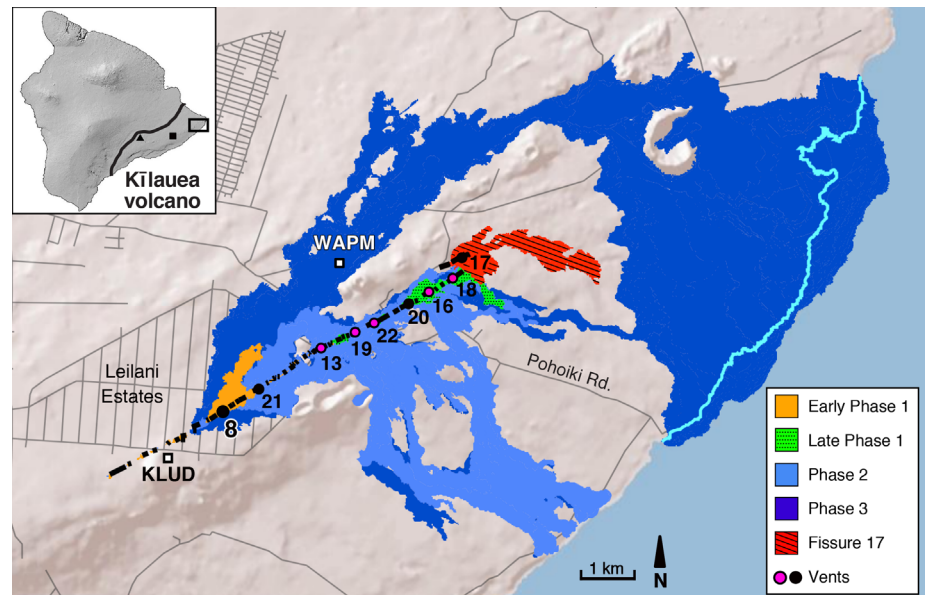

Fig. 1. Map of lava flows and vents from the 2018 Kīlauea eruption. Flows are color-coded by eruptive sequence: gold is lava from early phase 1 (initial fissures), stippled green is late phase 1 (early downrift fissures), striped red is fissure 17, light blue is phase 2 (flows of 17 to 27 May), dark blue is phase 3 (after 27 May). Numbers mark vent locations mentioned in text; magenta dots are reactivated fissures. The pre-eruption coastline is shown in light blue. Locations of tilt station WAPM and seismic station KLUD are shown as squares. Inset map shows the Island of Hawai'i and Kīlauea Volcano with the summit Halema'uma'u lava lake (black triangle) and Pu'u 'Ō'ō vent (black square) marked; map area is outlined. Map data: Esri, County of Hawaii, Hawaii Statewide GIS Program and USGS (25).

[1]Department of Geology, University of Hawai'i at Hilo, 200 W. Kawili Street, Hilo, HI 96720, USA. [2]U.S. Geological Survey, Hawaiian Volcano Observatory, 1266 Kamehameha Avenue, Suite A8, Hilo, HI 96721, USA. [3]Department of Geology and Geophysics, SOEST, University of Hawai'i at Mānoa, Honolulu, HI 96822, USA.
*Corresponding author. Email: gansecki@hawaii.edu

Early phase 1 (3 to 9 May, fissures 1 to 15, ~0.1% of total erupted volume) and late phase 1 (12 to 18 May, fissures 16, 18 to 20, 22, ~0.1% of total erupted volume) were both small-volume, short-lived fissures separated by a short eruptive pause and a shift downrift (Fig. 1). Phase 2 saw increased lava effusion that sent large flows to the southeast as fountaining migrated back uprift (17 to 27 May; fissures 21 to 24, others continue or reactivate, ~3 to 7% of total volume). During phase 3, voluminous output from fissure 8 vent produced a large and destructive channelized lava flow (28 May to 4 August; ~92 to 96% of total volume). Fissure 17 produced fountains, highly viscous lava flows, and explosive bursts (13 to 25 May; ~0.5 to 0.6% total volume).

Geochemical analysis

USGS-HVO field crews collected 113 molten or recently solidified samples during the eruption. Samples were delivered 2 to 12 hours after collection to UH Hilo, where they were dried, given a quick petrographic overview, and prepared for analysis (6). We analyzed all samples by energy-dispersive x-ray fluorescence spectroscopy (EDXRF) for a limited suite of whole-rock major (Ca, K, Ti, Mg) and trace (Rb, Sr, Zr, Y, Nb) elements (data S1) (7). The main advantages of EDXRF for geochemical monitoring are minimal sample preparation and rapid data production. The turnaround time from rock to data was 1 to 2 hours, and we analyzed most within 24 hours of field col-

lection. We analyzed a subset of samples during and after the eruption by conventional wavelength-dispersive X-ray fluorescence (WDXRF) spectroscopy for a full suite of elements (data S2) (7). We also determined matrix glass (data S3) (7) and phenocryst (data S4) compositions by electron microprobe analysis (EMPA) on polished thin sections and grain mounts from representative samples. Matrix glass compositions represent the melt component of magma.

Geothermometry

We calculated lava temperatures using Ca- or Mg-based geothermometers calibrated using Kīlauea glasses (7, 8). For initial estimates of lava temperature, we used the geothermometers on whole-rock, EDXRF-derived CaO or MgO. Because the equations were empirically derived from mineral-free glass, calculated temperatures will be biased high when Ca- or Mg-rich minerals are present and thus represent a maximum temperature (given as T_{CaOmax} and T_{MgOmax}). These estimates generally agreed within ~5°C; greater divergence is an indication of disequilibrium between the glass and mineral phases (9). EMPA analysis of matrix glass for MgO and CaO produces more accurate melt temperatures, but takes longer to obtain. T_{CaOG} and T_{MgOG} were generally 5° to 15C° cooler than T_{CaOmax} and T_{MgOmax} (Table 1) unless the sample was crystal-poor. Some samples showed larger differences, in particular the highly evolved and crystal-rich andesite from fissure 17.

Results

Early phase 1: Eruption of low-temperature, highly differentiated lavas (3 to 9 May 2018)

Highly differentiated basalt erupted from 15 fissures in or near the Leilani Estates subdivision during the first week of the eruption. Cooling and crystallization produce differentiated or evolved magmas enriched in "incompatible" elements (Zr, Nb, K, Ti, and others) not incorporated into crystals. Early phase 1 incompatible–trace-element concentrations (Zr and Nb) were twice that of average lava erupted during the past 35 years of activity on Kīlauea (Table 1, Fig. 2, and data S1). Compatible major elements MgO (Fig. 2) and CaO (Fig. 3) were low, giving a maximum temperature of ~1110°C, about 30° to 40°C lower than temperatures typical of previous Puʻu ʻŌʻō and Halemaʻumaʻu eruptions (Table 1). TiO$_2$ concentrations were much higher in this phase than any others (Fig. 4).

The whole-rock WDXRF analyses of SiO$_2$ [51.7 to 52.3 weight % (wt %)] and alkalis (Na$_2$O+K$_2$O = 3.8 to 4 wt %) confirmed values higher than typical Kīlauea compositions (10) and were classified as silica-rich tholeiitic basalt to borderline basaltic andesite (data S2).

We calculated representative melt temperatures of 1104°C from CaO and 1097°C from MgO on matrix glasses, which were about 10°C cooler than maximum temperatures calculated from EDXRF data. Glass SiO$_2$ compositions from the 2018 LERZ, as well as earlier Puʻu ʻŌʻō and summit samples, were mostly typical for Kīlauea tholeiitic basalts, averaging 50 to 51 wt %. Higher glass SiO$_2$ was only observed in two phase 1 samples, in addition to samples from fissure 17 and several reactivated fissures (data S3).

Rapidly cooled lava from early phase 1 was glassy and appeared mostly aphyric in hand specimen, but we identified 30 to 40% microlites with scanning electron microscopy (SEM). These crystals were mostly high–aspect ratio plagioclase laths 20 to 100μm in length. Larger, more equant phenocrysts of plagioclase and pyroxene up to 1 mm in size were also present. Plagioclase of An$_{52-65}$ was most common, though a few had more anorthitic cores (Fig. 5). Pyroxenes were mostly augite with some high-Mg orthopyroxene-pigeonite (~70% enstatite component) (fig. S1). Most phenocrysts showed strong normal zoning with more Mg-rich cores. Rare ilmenite and Fo$_{64-70}$ olivine (Fig. 5) were present in some samples.

Late phase 1: Eruption of higher-temperature, less-differentiated lavas (12 to 18 May 2018)

Tremor and deformation continued through the 9 to 11 May pause in eruptive activity, tracking migration of the dike 2 km eastward over 3 days (Fig. 3) (5). Beginning on 12 May, fissures 16, 18 to 20, and 22 erupted east of Pohoiki Road, downrift of the earlier fissures,

Table 1. Calculated average eruptive temperatures and representative incompatible-element compositions. Whole-rock Zr and Nb compositions, plus average whole-rock and glass temperatures from CaO and MgO glass thermometers (8). Bulk maximum temperatures from rapid-response EDXRF and WDXRF duplicates (in parentheses) generally agree within 2° to 3°C (data S1 and S2) (7). Glass temperatures from EMP analysis of MgO and CaO in matrix glass (data S3). Glass temperatures are lower than the bulk-rock temperatures, except in later phase 3 where few Ca-bearing crystals are present. The rapid-analysis temperatures show the same pattern as the glass: substantially cooler than Puʻu ʻŌʻō in early phase 1, higher temperature in late phase 1, then reaching Puʻu ʻŌʻō-like temperatures in phase 3.

Source	Bulk rock (max) temp.		Glass temp.		Zr (ppm)	Nb (ppm)
	T_{CaO} (°C)	T_{MgO} (°C)	T_{CaO} (°C)	T_{MgO} (°C)		
Halemaʻumaʻu lava lake	N/A*	(1160)	N/A	1155	140 (136)	12 (12)
Puʻu ʻŌʻō 2018	1149 (1152)	1148 (1154)	1144	1143	145 (138)	14 (13)
2018 LERZ Eruption:						
Early Phase 1	1111 (1113)	1107 (1111)	1104	1097	288 (283)	28 (27)
Late Phase 1	1128 (1131)	1130 (1132)	1113	1106	222 (213)	20 (19)
Phase 2	1144 (1143)	1158 (1160) †	1129	1126	169 (166)	16 (15)
Phase 3	1143 (1144)	1180 (1176) †	1142	1146	153 (146)	14 (13)
Fissure 17 explosive	1062 (1063)	1068 (1065)	1028	1033	543 (540)	41 (41)
Fissure 17 late flow	1093 (1098)	1088 (1096)	1079	1071	367 (365)	31 (31)
Reactivated F22	1097 (1103)	1093 (1108)	1084	1074	348 (329)	30 (28)
Reactivated F13	1115 (1117)	1114 (1119)	1094	1093	291 (284)	25 (24)

*Olivine only, T_{CaO} not applicable.   †Entrained (high-MgO) olivine makes temperature estimates too high.
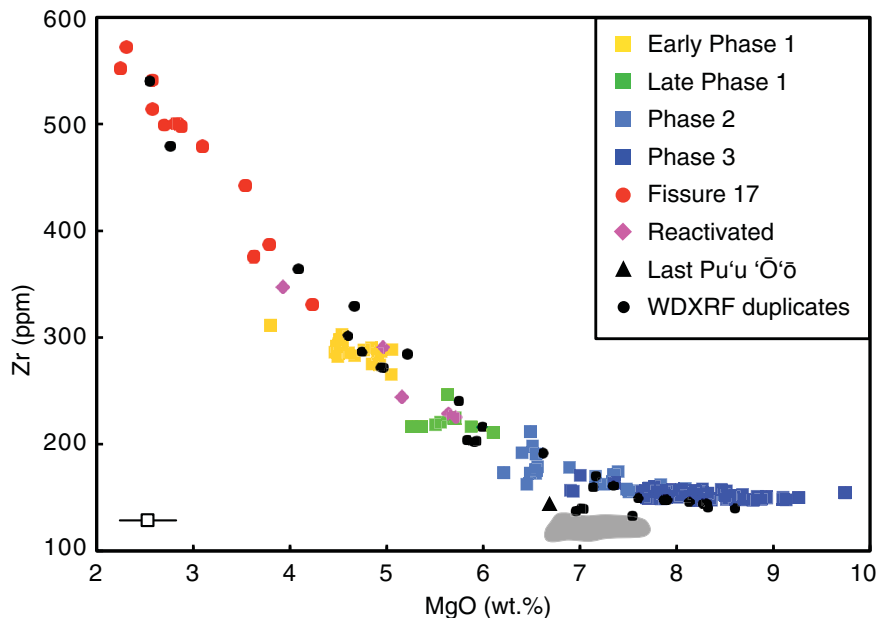
Fig. 2. Plot of incompatible element (Zr) versus a differentiation index (MgO) for all lava samples from the 2018 Kīlauea eruption. Data from whole-rock EDXRF (data S1) (7) except black circles are WDXRF data obtained on a subset of the same samples (data S2) (7). Datasets show good agreement despite relatively large error for MgO. Gray area is region of 2016–2018 values from Puʻu ʻŌʻō lava; black triangle is the last lava from Puʻu ʻŌʻō. Bar in lower left gives estimated EDXRF 1 SD MgO error of ±0.31 wt % (Zr 1 SD error of ±3 ppm is within symbol size).

but along the geophysically defined strike of the intrusion (Fig. 1).

The composition of the late phase 1 lava was promptly recognized as substantially less fractionated than the initial western fissure lava, having lower incompatible elements (Fig. 2 and Table 1), higher CaO (Fig. 3), and higher MgO (Fig. 2). The T_{CaOmax} of 1128°C was 15° to 20°C higher than early phase 1. MgO and CaO glass compositions yielded average temperatures of 1106° and 1113°C, respectively. Though hotter than the early phase 1 eruptions, late phase 1 lava was still 20° to 30°C cooler and less mafic than prior Puʻu ʻŌʻō or Halemaʻumaʻu lava (Table 1) (11).

Late phase 1 rocks contained 25 to 30% small (1 to 3 mm) plagioclase and pyroxene phenocrysts, with fewer 10- to 50-μm microlites in the glassy spatter compared to early phase 1 samples. Plagioclase compositions were mostly An_{55-65} from the first fissures in this sequence, increasing to An_{70} a few days later. Pyroxenes were mostly augite, and we identified only one orthopyroxene phenocryst. Intergrown clots of plagioclase and augite were common, and most of the pyroxenes showed sector and/or concentric zoning. Minor olivine of Fo_{68-75} was also present, reaching Fo_{78-79} in an early 18 May sample. Fissure 19, though active on 17 May, had anomalously high K_2O and low TiO_2, similar to some of the later reactivated fissures (Fig. 4).

Phase 2: Higher-temperature mafic mixed lava and increased effusion (17 to 27 May 2018)

We identified an abrupt change in chemistry on the afternoon of 17 May, when fissure 21 erupted more mafic lava in the middle of the western fissures in Leilani Estates. The following day, fissure 20 lava in the eastern group shifted from typical late phase 1 lava with ~6 wt % MgO and 225 parts per million (ppm) Zr in the morning, to 6.5 wt % MgO and 198 ppm Zr by evening of the same day (data S1) (7).

Between 18 and 26 May, effusion rates increased markedly at fissures 16, 18 to 20, and 22. Vents also became active again uprift, particularly fissures 6, 13, and 15 (Fig. 6). By 19 May, large, fast-moving lava flows from fissures 20 and 22 reached the ocean. We used EDXRF analysis to calculate T_{CaOmax} of 1138° to 1150°C (Fig. 3). Zr and MgO values approached Puʻu ʻŌʻō-like compositions, but T_{MgOmax} was anomalously high (Fig. 2 and Table 1). This was likely due to entrainment of high-MgO olivine crystals, out of equilibrium with the melt (9). Glass CaO and MgO temperatures agreed, averaging 1128°C.

The bulk composition of phase 2 lava was substantially less differentiated than previous samples. Whole-rock MgO ranged from 7 to 8 wt %, Zr from 175 to 150 ppm, and glass MgO increased from 4.7 to 6 wt % (Fig. 5). Considering the widespread spatial distribution of phase 2 vents, compositional

variability was moderate and most strongly correlated with time.

Phenocrysts, by contrast, ranged widely in composition, with plagioclase cores of up to An_{78} and rims as low as ~An_{60}. Olivine compositions ranged from Fo_{69} (rims) to Fo_{89} (cores), the latter values surpassing any from Puʻu ʻŌʻō or recent summit eruptions (Fig. 5). Pyroxene phenocrysts were mostly augite, but some pigeonite was also present, mostly in crystal cores (fig. S1). Cr-spinel inclusions, more common in Halemaʻumaʻu than Puʻu ʻŌʻō samples [e.g., (11)], were found in some of the high-Fo olivine phenocrysts.

Phase 3: Voluminous eruption of high-temperature mafic lava (28 May to 4 August 2018)

On 28 May, a massive outpouring of basalt began from fissure 8. These high-volume flows bear similarities in bulk composition, phenocryst assemblages, and temperature to Puʻu ʻŌʻō and summit lavas. Most element concentrations leveled out at values similar to those of recent tholeiitic basalt at Kīlauea (Figs. 2 and 3 and Table 1). T_{CaOmax} remained at 1142° to 1147°C for the rest of the eruption, with the exception of several reactivated fissures discussed below. Whole-rock MgO continued to vary, but increased to up to 9 wt %, higher than the ~7 wt % seen in the previous 10 years at Puʻu ʻŌʻō (Fig. 2), likely due to entrainment of high-MgO olivine. SiO_2 (~51 wt %), alkalis (~2.7 wt %), and most other major elements were similar, if proportionally lower than values of basalts erupted from Puʻu ʻŌʻō (data S2) (7).

We confirmed the presence of Mg-rich (Fo_{88-89}) olivine cores and crystals using the electron microprobe. Rims of most of the olivine crystals had lower Fo (Fo_{78-80}), closer to equilibrium with glass MgO concentrations averaging 6.3 wt % through the end of the eruption. These rim and glass values were similar to Puʻu ʻŌʻō compositions (Fig. 5). Glass temperatures were within a few degrees of T_{CaOmax} in most of these plagioclase-poor lava flows, with the exception of a few crystal-rich distal samples from late May and June (Fig. 5 and Table 1).

The phenocryst cargo of the lava changed from augite, plagioclase, and olivine, to near olivine-only in late June. Cr-spinel was more common in the later samples, mostly as inclusions in or in close association with high-Fo olivine phenocrysts. Plagioclase and pyroxene microlites were present in quenched samples, though in smaller proportion than in the earlier phases of the eruption.

Fissure 17: Eruption of highly evolved lava (13 to 25 May 2018)

Fissure 17 erupted through late phase 1 and 2 from an en echelon segment offset north of the main fissure trend and at the distal
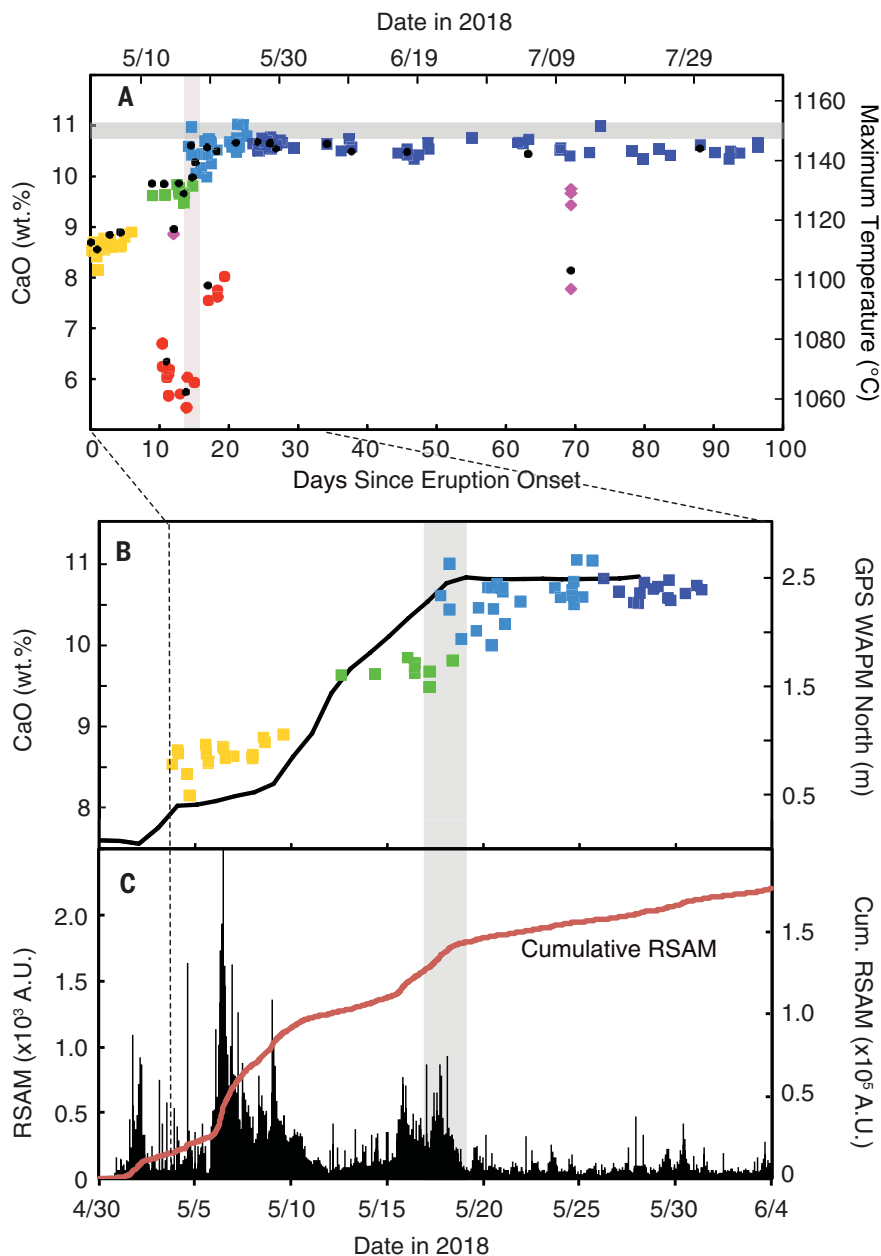
Fig. 3. Temporal variation of bulk CaO and maximum temperature and correlation with nearby deformation and seismicity. (**A**) Plot of whole-rock CaO wt % and calculated temperature variation over time during the 2018 eruption. Whole-rock CaO provides maximum temperature estimate using CaO-in-glass thermometer of (8). Data from EDXRF, black circles are duplicate analyses by WDXRF. Horizontal gray bar shows average Puʻu ʻŌʻō CaO composition over the previous 3 years (10.9 ± 0.2 wt %). Symbols as in Fig. 2. (**B**) Whole-rock CaO wt % as above superimposed on the northward motion of WAPM GPS station (right axis, black line). Dashed line is eruption onset, vertical gray bar indicates inferred arrival time of main intrusion. (**C**) Vertical black bars show 1-hour average of RSAM [Real-Time Seismic Amplitude Measurement (26) in arbitrary units A.U. on left axis] at the KLUD station. Red line is cumulative hourly RSAM on right axis. (B) and (C) are plotted over the period 30 April to 4 June 2018. Station locations shown in Fig. 1; WAPM was destroyed on 29 May.

northeastern end (Figs. 1 and 6). This was the only vent substantially offset (~200 m, Fig. 1) from the rest of the fissure system. The composition of this lava is more evolved than any previous known eruptions on Kīlauea Volcano, either from historic or prehistoric flows [e.g., (10)]. Zr concentrations were >500 ppm, and MgO was <3 wt % (Fig. 2 and Table 1). T_{CaOmax} reached low values of 1062° to 1093°C.

Whole-rock SiO_2 was 55 to 60 wt % with total alkalis of 4.5 to 5.7 wt % (data S2) (7),

classifying it as an andesite. The lava apparently became more evolved during the first few days of activity, then quickly changed to a less evolved, basaltic andesitic composition (Fig. 3). Matrix glass from fissure 17 andesite attained 67 wt % SiO_2 (data S3) near the end of late phase 1. Initial CaO and MgO glass temperatures were ~1050°C, dropping to 1030° to 1035°C in high-silica spatter samples, then increasing to 1070° to 1080°C in the last-erupted lava.

Phenocrysts were predominantly plagioclase and two pyroxenes, all with wide compositional ranges (Fig. 5 and fig. S1). Plagioclase and pyroxene microlites were also abundant. Unlike other lavas from the eruption, at least a few fissure 17 samples contained ilmenite, titanomagnetite, apatite, or rare inclusions of pyrrhotite, but no olivine. Inclusions, crystal clusters, and large, coarse-grained, glassy enclaves were common.

The western end of fissure 17 erupted more explosively than other vents. It is unclear how much of the explosivity was due to the high viscosity of the magma and how much was due to interaction with external groundwater, as the biggest explosions occurred on the west end, where the volumetric output was low and viscosity highest. Similar explosive behavior was not seen at other low-volume but less-differentiated fissures nearby. Activity at the central fissure 17 vent was predominantly fissure fountaining producing lava flows, simultaneous with explosions at the west end. The extremely viscous flow, with its high density and yield strength and intense radiative heat, made sampling challenging. Most spatter samples were collected 200 to 300 m from the explosive vent.

Reactivation of fissures: Eruption of mixed compositions

Many of the eruptive vents along the fissure system reactivated intermittently days to weeks after their initial cessation (Figs. 1 and 6). Several showed a change to more evolved rather than less evolved compositions, at least briefly. Fissure 13 reactivated on 15 May after being inactive for 6 days and produced lava with a bulk composition similar to that of its initial eruption, but with much higher matrix glass SiO_2 (54 to 55 wt % versus 49 to 51 wt %) and apatite, which was not found in any of the initial eruptions. Fe-rich orthopyroxene phenocryst compositions from this sample overlapped with fissure 17 compositions (fig. S1) and were unlike any other unit analyzed. The composition of lava from fissure 13 became less evolved with subsequent reactivations and, by 24 May, was indistinguishable from the composition of other phase 2 lava.

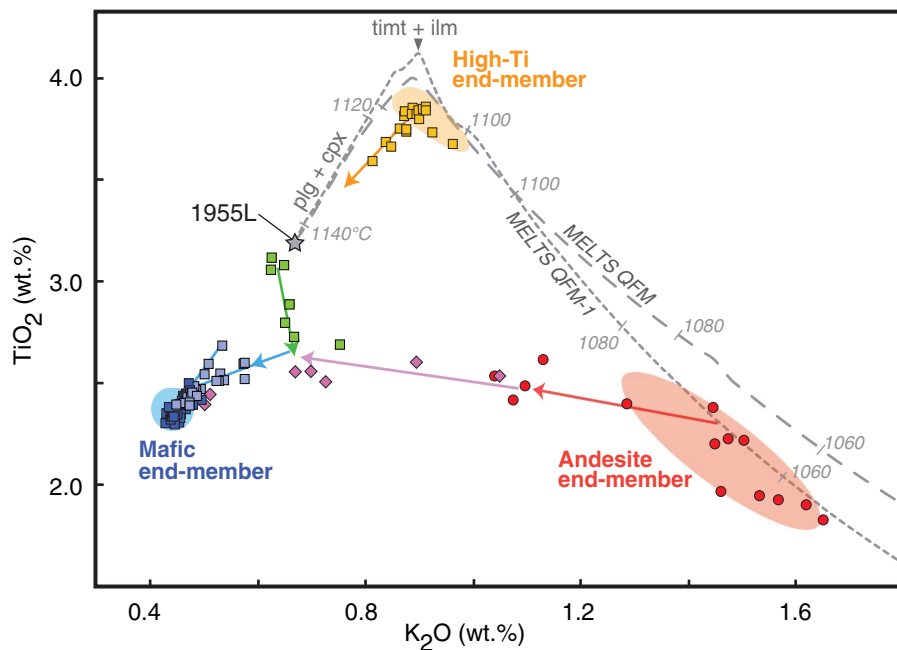Other fissures reactivated during late June (fissure 18) and early July (fissure 22). Samples

Fig. 4. K₂O versus TiO₂ plot of the 2018 eruption samples with possible mixing, end-members, and fractionation paths. Whole-rock EDXRF data [from data S1 (7)]. Symbols as in Fig. 2; colored regions distinguish inferred mixing end-members. Colored arrows show the direction of compositional change with time for each stage. Dashed lines are two MELTS (12, 27) fractional crystallization models performed using the bulk composition of late 1955 samples (24) as starting composition, at fO_2 conditions along the QFM and QFM-1 buffers. Temperature steps are shown and compare favorably with our calculated magma temperatures (Table 1).

were not collected until the eruption stopped, because the vents were inaccessible after the fissure 8 flow began, so their exact timing is unknown. Near-vent samples are given a maximum formation date of 12 July 2018. These samples all show anomalously evolved compositions compared to fissure 8 lavas from the same period (Figs. 2 to 4).

This change with reactivation was most pronounced at fissure 22, which produced audible explosions and built a cinder cone over the vent. The composition of vent spatter overlaps with that of the late-erupted fissure 17 lava (Figs. 2 to 4) and was thus quite viscous (table S1). Glass SiO₂ averaged 55.6 wt %, and MgO 3.0 wt %. Phenocryst compositions varied widely, overlapping with crystals from fissure 8 (Fo₇₈ olivine) and fissure 17 (high-Fe orthopyroxenes, An₅₀ plagioclase) lavas (Fig. 4 and fig. S1). Olivine compositions showed a an exceptionally wide range, from Fo₆₃ to Fo₈₀ (Fig. 5). Physical mingling of two distinct melts is visible in SEM images of fissure 22 spatter (fig. S2).

Interpreting magmatic processes

The 2018 Kīlauea eruption recorded a complex story of magma storage, mixing, and migration. During the past two-plus centuries, magma has repeatedly been injected into the LERZ (1790, 1840, 1924, 1955, and

1960; fig. S3), mixing with differentiated magmas from prior intrusions (1). Geochemical evidence suggests that at least two separate LERZ magma bodies interacted and mixed with hotter, less fractionated summit or deep rift zone magma during the 2018 eruption (Fig. 6). Early phase 1 lavas constitute one source (the "High-Ti" end-member of Fig. 4) and fissure 17 lavas a second stored magma source (the "Andesite" end-member). Phase 3 lavas represent another end-member, which appears to source from an olivine-controlled, tholeiitic basalt magma with similarities to both the Halemaʻumaʻu and Puʻu ʻŌʻō lavas ("Mafic" end-member).

Differentiated and stored magmas

Whole-rock and mineral compositions of initial phase 1 lavas ("High-Ti" end-member) form distinct clusters and showed little to no overlap with other erupted lavas or Puʻu ʻŌʻō and summit lavas (Figs. 2 to 5 and fig. S1). The evolved composition, low temperature, and presence of orthopyroxene indicate early phase 1 differentiated from magma previously trapped in the rift zone [e.g., (1)] that was forced to the surface by the intruding dike (Fig. 3). Most early phase 1 lavas could have formed by differentiation of late 1955 magma (Fig. 4), on the basis of MELTS calculations (12). The rare presence of ilmenite agrees with

this model, which shows the basalts to be at maximum iron enrichment and onset of Fe-Ti oxide crystallization. Several early phase 1 samples were either less differentiated or lie along a possible mixing line with later phase 1 compositions (Fig. 4). Late phase 1 lavas were too mafic to be differentiated from 1955 lava (Fig. 4), and mineralogical and compositional variations indicate that they were likely mixtures between the three magmatic end-members.

The fissure 17 andesite flows had a broad range of orthopyroxene Mg compositions from enstatite 80 to 45 (fig. S1). The distinctive mineralogy and chemistry suggested the andesite formed as an isolated magma body rather than by mixing with other magmas. We considered that the andesite resulted from mixing between a dacite body encountered during drilling in 2005 by Puna Geothermal Venture about 2 km away (13) and one of the other end-members. However, the andesite does not sit on any reasonable mixing lines with the dacite (data S2 and fig. S4).

Late 1955 magma is also a possible source for the andesite, depending on cooling history and oxygen fugacity (fO_2) conditions (Fig. 4). It cannot be the source of both the andesite and the early phase 1 lava, as the compositional gap is too great and the andesite volume much larger. We could not obtain reasonable matches between MELTS differentiation paths and the andesite using other characterized local magma sources in the LERZ (1960 or 1790) as starting compositions (Fig. 4). A specific source may not be identifiable if larger, long-lived rift magma bodies were amalgamations of repeated dike injections over centuries within the lower east rift zone (14, 15).

Mixing and hybridization of lavas

Lavas erupted during late phase 1 and phase 2 appeared to be part of a continuum of mixing between early phase 1 and phase 3 compositions (Figs. 2, 3, and 5). Simple mixing and hybridization would appear as a straight line between the High-Ti and Mafic end-members (Fig. 4) if it were caused by a mafic dike intruding a single differentiated rift stored magma body (1, 2).

Many late phase 1 and early phase 2 lavas showed unexpected signs of mixing with the fissure 17 andesite (Figs. 4 and 6). Lava collected from vents 20, 19, and 13 on 15 to 18 May, just prior to the onset of high-volume phase 2 eruptions, showed increasing mixing with the andesite, despite being up to 2.5 km from fissure 17 (Figs. 1 and 4 and data S1). The final four samples of andesite erupted on 20 to 22 May had about 25% lower K₂O, indicating mixing with mafic magma from the main dike system (Fig. 4). Vents 18 and 22 reactivated during phase 3, and their compositions also lie on a mixing line with the andesite
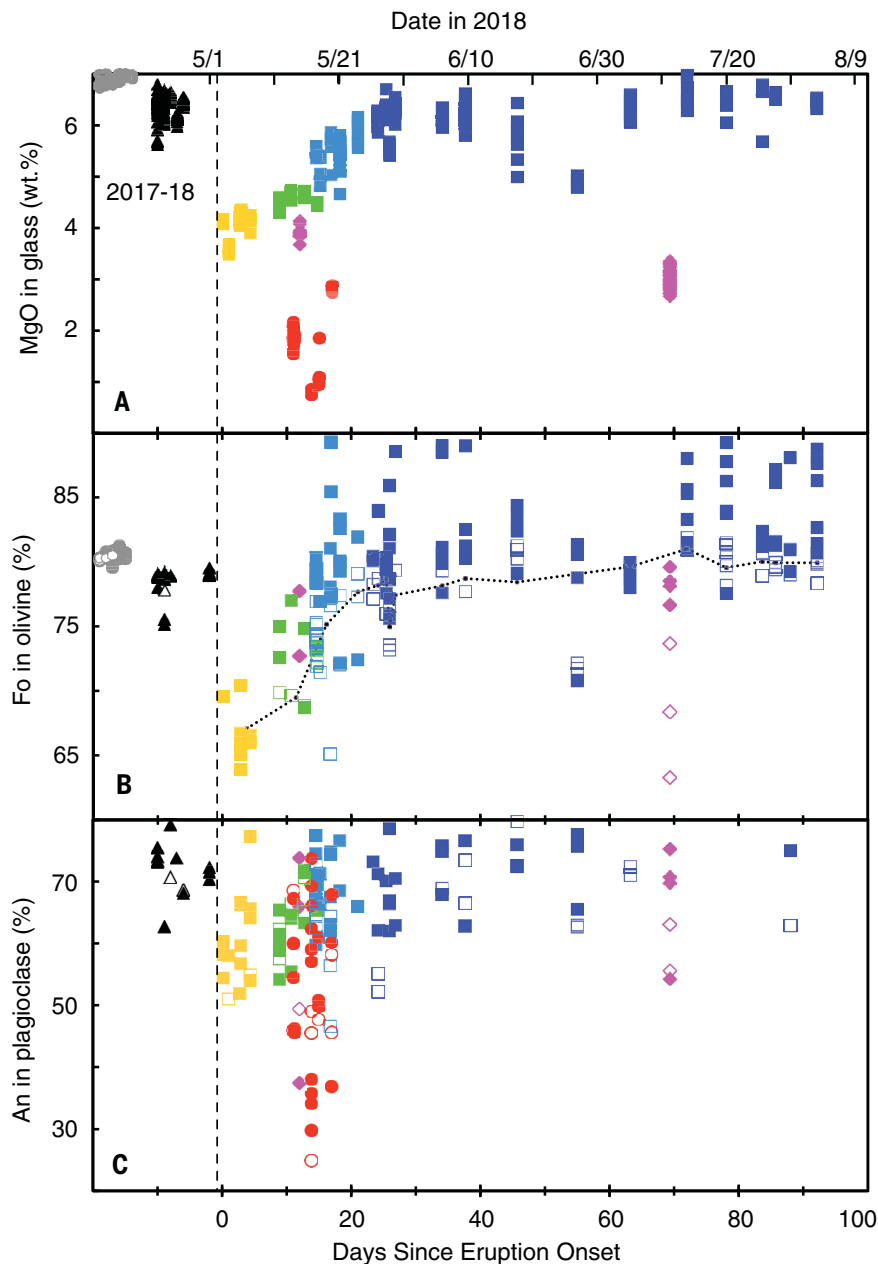
Fig. 5. Temporal variation in glass and mineral compositions. Plot of (**A**) MgO in matrix glass, (**B**) Fo mol % in olivine, and (**C**) An mol % in plagioclase during the 2018 eruption. To left of dashed line are compositions from Pu'u 'Ō'ō and Halema'uma'u lake lava from 2017–2018, including a breakout on Pu'u 'Ō'ō 2 days before the LERZ eruption began. Symbols are as in Fig. 2, with the addition of gray circles for summit samples. For the phenocryst analyses, open symbols are rims, solid are mineral cores. Dotted line in (B) is approximate Fo in equilibrium with maximum glass MgO in (A) using calculations of (*16*); note correlation with rim compositions. Glass MgO is very low in the initial phase 1 lava, increases until about 26 May, then levels out at approximately Pu'u 'Ō'ō levels, with the notable exception of fissure 17 and the anomalous reactivated fissures. One fissure 8 flow sample at day 55 is also anomalously low in glass and olivine MgO, but it was collected 12 km from the vent and is crystal-rich; other samples were collected within a few kilometers of their vents. Data from EMP spot-analyses (data S3 and S4) (*7*).

(Fig. 4 and data S1). One fissure 22 sample contained low-Mg orthopyroxenes (fig. S1), and Fe-Ti oxides found only in the andesite, and showed mingling between basalt and andesite glasses (fig. S2). The complex mixing patterns indicate that fissure 17 must be an en echelon fissure that intersected the andesite body but was also connected at depth to the main dike. The areal distribution of mixing (Fig. 6) suggests that the fissure 17 dike

system may extend at depth several kilometers to the southwest of the surface vent (Fig. 1) and that the andesite body could be larger than the erupted volume.

The arrival of clearly identifiable mafic magma in the intruding dike began on 17 to 18 May at the start of phase 2, marked by an abrupt rise in lava temperature, a shift in composition, rapidly increasing effusion rates, and the diminishing of local deformation and seismicity (Figs. 2, 3, and 5). Both new and reactivated fissures along the main trend showed rapid compositional fluctuations, as more primitive magma mixed with and flushed out the stored magma by 24 May. Extremely Mg-rich olivine crystals (Fo_{88-89}) first appeared on 20 May. The Fo_{88-89} olivine cores would have formed at temperatures of 1270° to 1290°C in magma with ~13 to 14 wt % MgO (*8*, *16*), conditions that generally only occur in the summit magma reservoir or possibly in the deep rift. The outer rims of the olivine crystals were around Fo_{75}, generally in equilibrium with the erupted lavas (Fig. 5B). Kink banding was observed in a few larger (>2 mm) olivines during phase 2, implying minor entrainment from a cumulate source, likely from a deeper part of the rift zone (*17*).

Voluminous mafic lava

Phase 3 lavas erupted from fissure 8 were reasonably homogeneous basalts similar in bulk composition to recent Pu'u 'Ō'ō or Halema'uma'u lava, but with distinctly elevated incompatible-element concentrations (K_2O, La, Ti, Zr) (Table 1 and Figs. 2, 4, and 7). As phase 3 progressed, MgO in glass shifted to higher values (from ~6.1 wt % to 6.6 wt %), and the mineral phenocryst assemblage gradually changed from olivine, clinopyroxene, and plagioclase to nearly olivine-only during the last month. Olivines in early phase 3 continued to show the broad range of core compositions (Fo_{77-89}) that were first observed in phase 2. Most olivine rims (Fo_{77-80}) were in equilibrium with the host melts (Fig. 5B) as they became more MgO-rich over time. The persistent high-Mg olivines (Fo_{88-89}) that we found in phase 3 lavas contained Cr-spinel, were normally zoned, and had euhedral forms, characteristics of a magmatic rather than rift cumulate origin. Olivines with Fo_{89} compositions are extremely rare in subaerial Kīlauea magmas (*11*, *18*), but have been found in the submarine portion of the East Rift zone (*17*), transported from either the summit magma reservoir or the deep rift zone.

Kīlauea magma compositions and summit storage

Magma ascends from the mantle into the summit storage system of Kīlauea with a recharge rate of at least 0.1 km³/year (*19*). The system was composed of a shallow (1- to 2-km depth),
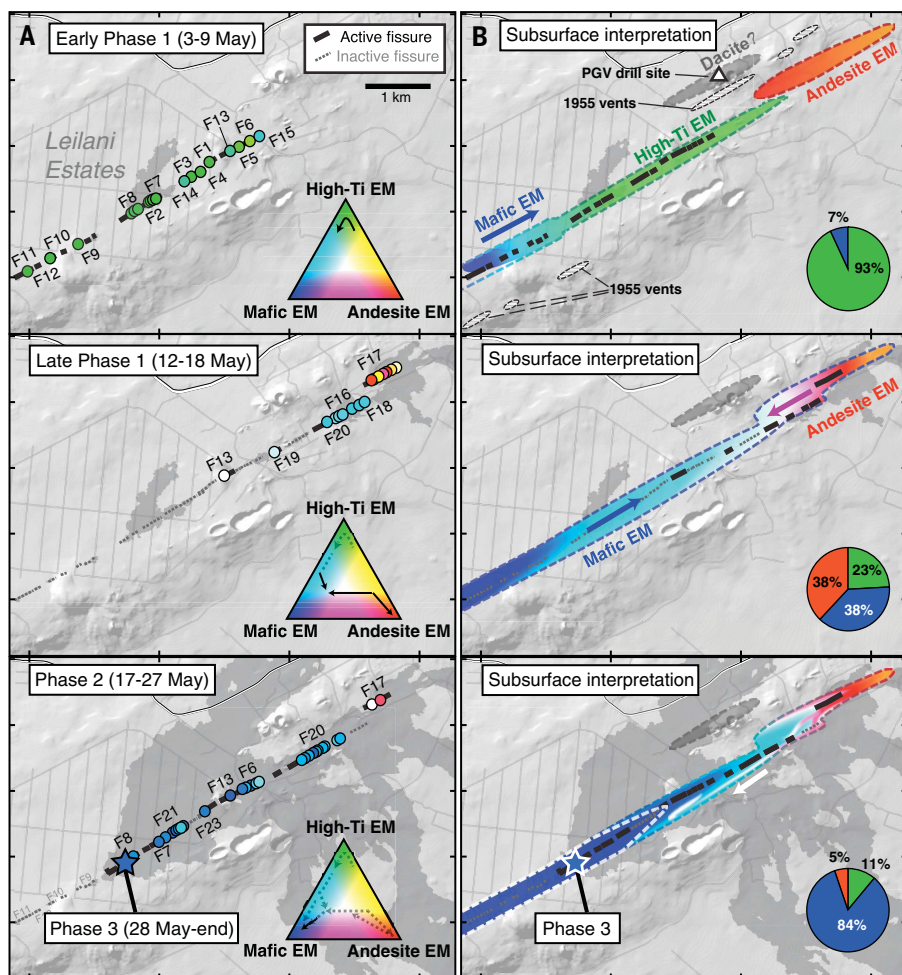
Fig. 6. Evolution of magma compositions with spatial location. (**A**) Series of panels showing samples repositioned along their active fissure of origin (colored circles) for each of the four phases (early and late phase 1, 2, 3), where the along-fissure position is approximated. A red-green-blue color mixing scheme is used to represent mixing of the three main end-member magmas. Note that the High-Ti end-member magma is green here (gold in other figures). RGB triangle shows color scheme and inferred mixing paths for the different periods. (**B**) Interpretative magma location maps corresponding to the same four phases. Colored regions represent the possible extent of magma underneath the surface. Colors show extents of mixing between end-members. Only general trends are depicted, as complex compositional variations occurred even within each of phases 1 and 2. Pie charts show percentages of each magma end-member erupted for each phase calculated from the TiO$_2$-K$_2$O relationships.

small magma chamber under Halemaʻumaʻu connected to a deeper (3 to 5 km), larger (3 to 20 km^3) chamber beneath the southeastern region of Kīlauea caldera with possible additional storage in a deep rift system (*19*, *20*). From 2008 to 2018, lava circulated, cooled, and degassed within the shallow Halemaʻumaʻu lava lake prior to passing back through the deeper chamber and out through a shallow dike (2- to 3-km depth) feeding the Puʻu ʻŌʻō vent (*11*, *19*). The volume of the 2018 summit collapse suggests that ~1 km^3 of magma was drained from the shallow Halemaʻumaʻu body (*5*).

Isotopic (Sr, Nd, Pb) and incompatible-element (K, Ti, Zr, La, Nb) compositions of olivine-controlled Kīlauea summit magmas

vary over time and are thought to reflect changes in mantle source compositions (*21*). Distinct changes in incompatible-element concentrations of olivine-fractionated summit and rift lavas have been previously attributed to (i) storage of small, discrete magma "batches" in a plexus of dikes and sills with residence times of one to two decades (*18*); (ii) nearly continual mantle recharge of a small summit magma chamber (<0.5 km^3) with a residence time of <10 years (*21*); and (iii) a compositionally and thermally zoned magma chamber with variable vertical mixing (*17*) and much longer residence times.

Incompatible-element concentrations of K$_2$O and TiO$_2$ (Fig. 7) in olivine-fractionated

Puʻu ʻŌʻō lavas (>6.8% MgO) gradually declined from 1985 to 2000, remained relatively flat through 2015, and began increasing systematically from 2016 to 2018. The correlation of Halemaʻumaʻu and Puʻu ʻŌʻō K$_2$O and TiO$_2$ values from 2010 to 2018 (Fig. 7) supports the genetic linkage between the two vents (*11*). The gradual change in composition coupled with the large erupted volume (~3.5 km^3) from 1983 to 2018 cannot be explained by the "dikes and sills" model but is compatible with the other two models. K$_2$O, TiO$_2$, Zr, and other incompatible elements were higher at the start of phase 3 than for the past 2 years (Figs. 2 and 7) and remained relatively constant for the remainder of the 2018 eruption. The small magma chamber model (<0.5 km^3) cannot easily explain the appearance of nearly 1 km^3 of "new" magma and disappearance of an equal volume of "Halemaʻumaʻu" magma. A more likely model is that denser, degassed magma draining from the shallow Halemaʻumaʻu chamber vertically mixed with hotter magma bearing a higher incompatible signature (K$_2$O, TiO$_2$, Zr,) residing either deeper in the summit chamber or the deep rift zone.

Magma transport

Early phase 3 lavas had olivine cores with distribution peaks at Fo$_{78-79}$ (similar to 2017–2018 Puʻu ʻŌʻō cores), at Fo$_{80-81}$ (similar to 2017–2018 Halemaʻumaʻu cores), and at Fo$_{88-89}$ (data S4 and fig. S5), representative of a higher-temperature component. This suggests that cooler magmas similar to Halemaʻumaʻu and Puʻu ʻŌʻō magmas were mixing with deeper, hotter lava in the summit chamber or deep rift to form the dike magma. During the last 20 days of the 2018 eruption, olivine cores show bimodal peaks at Fo$_{80-81}$ and Fo$_{88-89}$ (data S4 and fig. S5) with only a few Fo$_{78-79}$ cores. The combination of the distribution of olivine compositions, the absence of phenocrysts other than olivine, and the higher glass MgO compositions are highly suggestive that lavas erupted during the last 20 days were derived by mixing of shallow (cooler with lower K$_2$O) and deep (hotter with higher K$_2$O) components from the summit.

The initial dike propagated downrift from Puʻu ʻŌʻō on 30 April 2018 and erupted on 3 May. By 24 May, the mafic magma reached a stable, olivine-controlled composition with elevated incompatible-element concentrations relative to Puʻu ʻŌʻō and Halemaʻumaʻu lavas (Figs. 2, 5, and 7). The 3- to 4-week arrival time for mafic magma is consistent with intervals documented in 1955 and 1960. However, the final volume of mafic lava erupted in 2018 was about 10 times larger than the previous eruptions (*1*, *2*, *18*) and appears to have flushed the system of differentiated magma. It is unclear if magma was transported from
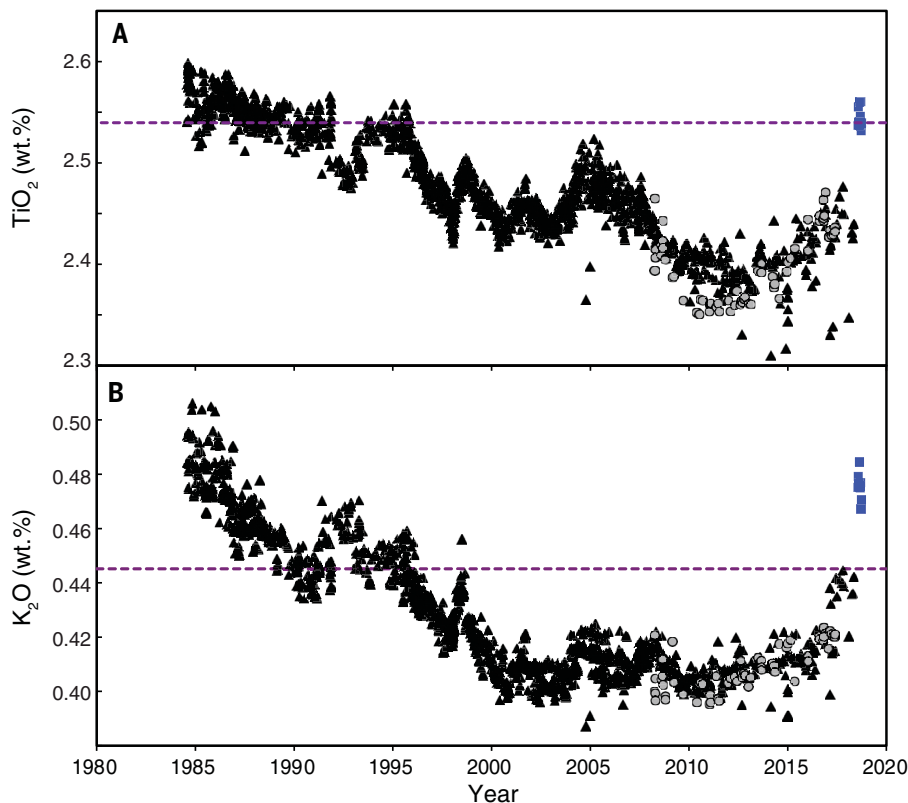
Fig. 7. Temporal variation of TiO₂ and K₂O during 1983–2018 Kīlauea eruptions. Whole-rock (**A**) TiO_2 and (**B**) K_2O (both normalized to 7 wt % MgO) are plotted versus time. Obviously evolved magmas (less than 6.8 wt % MgO) are excluded. Black triangles are Pu'u 'Ō'ō, gray circles are Halema'uma'u lava lake, and blue squares are 2018 LERZ fissure 8 samples; dashed line marks the average composition of the April and September 1982 summit eruptions [data from (28, 29)]. TiO_2 and K_2O by WDXRF; from (7, 11) (data S2).

the summit to the eruption site using the established Pu'u 'Ō'ō dike system at about 2- to 3-km depth (22) or if transport switched to the deep rift plumbing system (19, 20). The most magnesian olivines from the Pu'u 'Ō'ō eruption were Fo_{87} (23), suggesting that the abundant Fo_{88-89} olivines could not have been entrained by transport through the shallow Pu'u 'Ō'ō dike system. The Fo_{88-89} olivines may have originated from deeper parts of the rift system, picked up during transport (17). Alternatively, magma carrying the high-Fo olivines could have exited from a deeper level of the summit chamber directly into the deep rift system (17) (fig. S3).

Petrology as a volcano-monitoring tool

The use of near-real-time compositional data was incorporated into the eruption monitoring and response. Geochemical results were reported to HVO staff and posted on the communications platform for field crews when the data seemed relevant for response purposes. Early phase 1 lava was cool and contained abundant plagioclase microlites, indicating highly viscous lava (approximate bulk magma viscosity 6600 Pa·s, table S1)

that was likely to behave as slow-moving flows. Late phase 1 lava was 10° to 15°C hotter and had fewer microlites. The viscosity (2900 Pa·s) was lower, but the lava was still sluggish, and we anticipated the arrival of hotter and less viscous magma from Pu'u 'Ō'ō or the summit reservoir. The lava chemistry gave us early indication of hotter lava on 13 May, and we alerted science and field teams to the change. The 17 to 18 May arrival of less evolved and much hotter magma was indicated by bulk-rock MgO and CaO reaching Pu'u 'Ō'ō compositions. Field crews were again alerted that the substantial compositional change was underway and could lead to greater effusion of hotter, more fluid lava. Phase 2 and 3 lavas (~1140° to 1150°C) had viscosities in the typical range for 'a'ā and pāhoehoe (~1150 Pa·s), increasing the likelihood of faster-moving flows. The chemical shifts correlated well with deformation and seismic signals recorded on nearby stations, showing the expansion of the dike (northward movement) essentially leveling out around that same time (Fig. 3).

A similar, if less extreme, eruptive sequence occurred during the 1955 LERZ eruption (24),

implying that future rift zone eruptions may start deceptively small as older, stored magma erupts. Once the magma pathway opens, and fresher, hotter magma arrives, rift zone eruptions can rapidly switch to large, fast-moving lava flows.

The explosive nature of fissure 17 lava was also consistent with its unusually evolved chemistry. The viscosities we calculated were orders of magnitude higher than for other units (up to ~2 × 10⁶ Pa·s).

A critical part of a volcano response is outreach and communications with the public. HVO's communications included geochemical information in press releases, interviews, and social media posts, and found an audience surprisingly interested in the seemingly esoteric questions of "new" and "old" magma sources and transport within Kīlauea.

Conclusion

The 2018 eruption of Kīlauea Volcano provided an opportunity to test a rapid-response geochemical analysis routine developed during the continuous eruption at Pu'u 'Ō'ō. The effort yielded critical information for hazards assessment and risk mitigation during the eruption. The collection of this large suite of lava samples and rich geochemical data set also allowed estimates of magma composition, mixing, temperature, viscosity, and travel time down the rift zone. Notably, the rapid-response data also proved highly suitable for geochemical modeling. The extremely large sample set that was made possible by our strategy filled in many gaps and allowed us to construct a more complete picture of the complex lava interactions. Based on the success of the HVO-UH Hilo geochemistry monitoring collaboration, other volcano observatories may benefit from similar efforts.

Materials and methods

USGS-HVO field crews collected 113 molten or recently solidified samples during the eruption. Samples were delivered 2 to 12 hours after collection to UH Hilo, where they were dried, given a quick petrographic overview, powdered, and pressed into pellets for analysis. We analyzed all samples by EDXRF for a limited suite of major (Ca, K, Ti, Mg) and trace (Rb, Sr, Zr, Y Nb) elements in the whole rock. The turnaround time from rock to data was 1 to 2 hours, and we analyzed most within 24 hours of field collection. We analyzed a subset of samples during and after the eruption by conventional WDXRF spectroscopy for a full suite of elements. CaO and MgO concentrations were used as geothermometers to estimate magma temperatures. We also determined matrix glass and phenocryst compositions by EMPA on polished thin sections and grain mounts from representative samples.

REFERENCES AND NOTES

1. T. L. Wright, R. S. Fiske, Origin of the differentiated and hybrid lavas of Kilauea Volcano, Hawaii. *J. Petrol.* **12**, 1–65 (1971). doi: 10.1093/petrology/12.1.1

2. R. T. Helz, T. L. Wright, Differentiation and magma mixing on Kilauea's east rift zone: A further look at the eruptions of 1955 and 1960. Part I. The late 1955 lavas. *Bull. Volcanol.* **54**, 361–384 (1992). doi: 10.1007/BF00312319

3. M. O. Garcia, R. A. Ho, J. M. Rhodes, E. W. Wolfe, Petrologic constraints on rift-zone processes: Results from episode 1 of the Puʻu ʻŌʻo eruption of Kīlauea volcano, Hawaiʻi. *Bull. Volcanol.* **52**, 81–96 (1989). doi: 10.1007/BF00301548

4. C. R. Thornber, "Magma-reservoir processes revealed by geochemistry of the Puʻu ʻŌʻō - Kūpaianaha Eruption" in *The Puʻu ʻŌʻō – Kūpaianaha Eruption of Kīlauea Volcano, Hawaiʻi: The First 20 Years*, C. Heliker, D. A. Swanson, T. J. Takahashi, Eds., U.S. Geol. Survey Prof. Paper **1676**, 121–136 (2003).

5. C. A. Neal et al., The 2018 rift eruption and summit collapse of Kīlauea Volcano. *Science* **363**, 367–374 (2019). doi: 10.1126/science.aav7046; pmid: 30538164

6. Materials and methods are available as supplementary materials.

7. R. L. Lee et al., Whole-rock and glass chemistry of lava samples collected during the 2018 Lower East Rift Zone eruption of Kilauea. U.S. Geol. Surv. Data Release, https://doi.org/10.5066/P9LVY7GV (2019).

8. R. T. Helz, C. R. Thornber, Geothermometry of Kilauea Iki lava lake, Hawaii. *Bull. Volcanol.* **49**, 651–668 (1987). doi: 10.1007/BF01080357

9. R. T. Helz, N. G. Banks, C. Heliker, C. A. Neal, E. W. Wolfe, Comparative geothermometry of recent Hawaiian eruptions. *J. Geophys. Res.* **100** (B9), 17637–17657 (1995). doi: 10.1029/95JB01309

10. E. W. Wolfe, J. Morris, Sample data for the geologic map of the island of Hawaii. *USGS Miscellaneous Investigations Series* **I-2524-B**, scale 1:100,000. https://doi.org/10.3133/i2524B (1996).

11. C. R. Thornber, T. R. Orr, C. Heliker, R. P. Hoblitt, "Petrologic testament to changes in shallow magma storage and transport during 30+ years of recharge and eruption at Kīlauea Volcano, Hawaiʻi" in *Hawaiian Volcanoes: From Source to Surface*, R. J. Carey, V. Cayol, M. P. Poland, D. Weis, Eds. Am. Geophys. Union, Geophys. Monograph **208**, 147–188 (2015).

12. M. S. Ghiorso, R. O. Sack, Chemical mass transfer in magmatic processes. IV. A revised and internally consistent thermodynamic model for the interpolation and extrapolation of liquid-solid equilibria in magmatic systems at elevated temperatures and pressures. *Contrib. Mineral. Petrol.* **119**, 197–212 (1995). doi: 10.1007/BF00307281

13. W. Teplow et al., Dacite melt at the Puna Geothermal Venture Wellfield, Big Island of Hawaii. *GRC Trans.* **33**, 989–994 (2009).

14. R. B. Moore, Distribution of differentiated tholeiitic basalts on the lower east rift zone of Kilauea Volcano, Hawaii. *Geology* **11**, 136–140 (1983). doi: 10.1130/0091-7613(1983)11<136:DODTBO>2.0.CO;2

15. K. M. Cooper, M. R. Reid, M. T. Murrell, D. A. Clague, Crystal and magma residence at Kilauea Volcano, Hawaii: ^{230}Th-^{226}Ra dating of the 1955 east rift eruption. *Earth Planet. Sci. Lett.* **184**, 703–718 (2001). doi: 10.1016/S0012-821X(00)00341-1

16. P. L. Roeder, R. F. Emslie, Olivine-liquid equilibrium. *Contrib. Mineral. Petrol.* **29**, 275–289 (1970). doi: 10.1007/BF00371276

17. D. A. Clague, J. G. Moore, J. E. Dixon, W. B. Friesen, Petrology of submarine lavas from Kilauea's Puna Ridge, Hawaii. *J. Petrol.* **36**, 299–349 (1995). doi: 10.1093/petrology/36.2.299

18. R. T. Helz, D. A. Clague, T. W. Sisson, C. R. Thornber, "Petrologic Insights into Basaltic Volcanism at Historically Active Hawaiian Volcanoes" in *Characteristics of Hawaiian Volcanoes*. U.S. Geol. Surv. Prof. Pap. **1801**, 237–262 (2014).

19. M. P. Poland, A. Miklius, E. K. Montgomery-Brown, "Magma supply, storage, and transport at shield-stage Hawaiian volcanoes" in *Characteristics of Hawaiian Volcanoes*. U.S. Geol. Surv. Prof. Pap. **1801**, 179–234 (2014).

20. P. T. Delaney, R. S. Fiske, A. Miklius, A. T. Okamura, M. K. Sako, Deep magma body beneath the summit and rift zones of Kilauea Volcano, Hawaii. *Science* **247**, 1311–1316 (1990). doi: 10.1126/science.247.4948.1311; pmid: 17843792

21. A. J. Pietruszka, D. E. Heaton, J. P. Marske, M. O. Garcia, Two magma bodies beneath the summit of Kīlauea Volcano unveiled by isotopically distinct melt deliveries from the mantle. *Earth Planet. Sci. Lett.* **413**, 90–100 (2015). doi: 10.1016/j.epsl.2014.12.040

22. A. T. Okamura, J. J. Dvorak, R. Y. Koyanagi, W. R. Tanigawa, "Surface deformation during dike propagation" in *The Puʻu ʻŌʻō Eruption of Kīlauea Volcano, Hawaiʻi: Episodes 1 through 20, January 3, 1983 through June 8, 1984*, E. W. Wolfe, Ed., U.S. Geol. Survey Prof. Paper **1463**, 165-180 (1988).

23. M. O. Garcia, J. M. Rhodes, E. W. Wolfe, G. E. Ulrich, R. A. Ho, Petrology of lavas from episodes 2-47 of the Puʻu ʻŌʻō eruption of Kīlauea Volcano, Hawaiʻi: Evaluation of magmatic processes. *Bull. Volcanol.* **55**, 1–16 (1992). doi: 10.1007/BF00301115

24. G. A. Mcdonald, J. P. Eaton, Hawaiian volcanoes during 1955. *U.S. Geol. Surv. Bull.* **1171** (1964).

25. Hawaiian Volcano Observatory staff, Preliminary map of the 2018 lower East Rift Zone eruption of Kīlauea Volcano, Island of Hawaiʻi. U.S. Geological Survey, https://doi.org/10.5066/P9940GY8 (2018).

26. E. T. Endo, T. Murray, Real-time Seismic Amplitude Measurement (RSAM): A volcano monitoring and prediction tool. *Bull. Volcanol.* **53**, 533–545 (1991). doi: 10.1007/BF00298154

27. P. D. Asimow, M. S. Ghiorso, Algorithmic modifications extending MELTS to calculate subsolidus phase relations. *Am. Mineral.* **83**, 1127–1132 (1998). doi: 10.2138/am-1998-9-1022

28. M. O. Garcia, A. J. Pietruszka, J. M. Rhodes, A petrologic perspective of Kīlauea volcano's summit magma reservoir. *J. Petrol.* **44**, 2313–2339 (2003). doi: 10.1093/petrology/egg079

29. A. J. Pietruszka, M. O. Garcia, A rapid fluctuation in the mantle source and melting history of Kīlauea Volcano inferred from the geochemistry of its historical summit lavas (1790-1982). *J. Petrol.* **40**, 1321–1342 (1999). doi: 10.1093/petroj/40.8.1321

SUPPLEMENTARY MATERIALS

science.sciencemag.org/content/366/6470/eaaz0147/suppl/DC1
Materials and Methods
Figs. S1 to S5
Table S1
Databases S1 to S4
References (30–37)

Science

The tangled tale of K#lauea's 2018 eruption as told by geochemical monitoring

Cheryl GanseckiR. Lopaka LeeThomas SheaSteven P. LundbladKen HonCarolyn Parcheta

Caldera collapse and flank eruption

Real-time monitoring of volcanic eruptions involving caldera-forming events are rare (see the Perspective by Sigmundsson). Anderson *et al.* used several types of geophysical observations to track the caldera-forming collapse at the top of K#lauea Volcano, Hawai'i, during the 2018 eruption. Gansecki *et al.* used near–real-time lava composition analysis to determine when magma shifted from highly viscous, slow-moving lava to low-viscosity, fast-moving lava. Patrick *et al.* used a range of geophysical tools to connect processes at the summit to lava rates coming out of far-away fissures. Together, the three studies improve caldera-collapse models and may help improve real-time hazard responses.

Science, this issue p. eaaz0147, p. eaay9070; p. eaaz1822; see also p. 1200

View the article online
https://www.science.org/doi/10.1126/science.aaz0147
Permissions
https://www.science.org/help/reprints-and-permissions

Use of think article is subject to the Terms of service